IJMMM International Journal of Minerals, Metallurgy and Materials 矿物冶金与材料学报（英文版）

Enhancing electrochemical performance and magnetic properties of $FeVO_4$ nanoparticles by Ni-doping: The role of Ni contents

Jessada Khajonrit, Thongsuk Sichumsaeng, Pinit Kidkhunthod, Supree Pinitsoontorn, Niwat Hemha, Kittima Salangsing, Anissa Srisongmueang, and Santi Maensiri

Cite this article as:
Jessada Khajonrit, Thongsuk Sichumsaeng, Pinit Kidkhunthod, Supree Pinitsoontorn, Niwat Hemha, Kittima Salangsing, Anissa Srisongmueang, and Santi Maensiri, Enhancing electrochemical performance and magnetic properties of $FeVO_4$ nanoparticles by Ni-doping: The role of Ni contents, *Int. J. Miner. Metall. Mater.*, 32(2025), No. 4, pp. 944-953. https://doi.org/10.1007/s12613-024-3019-0

View the article online at SpringerLink or IJMMM Webpage.

INTERNATIONAL JOURNAL OF
Minerals, Metallurgy and Materials

Volume 32, Number 4, April 2025
Page 944

Research Article https://doi.org/10.1007/s12613-024-3019-0

Enhancing electrochemical performance and magnetic properties of $FeVO_4$ nanoparticles by Ni-doping: The role of Ni contents

Jessada Khajonrit[1),✉], *Thongsuk Sichumsaeng*[2)], *Pinit Kidkhunthod*[3)], *Supree Pinitsoontorn*[4)], *Niwat Hemha*[5)], *Kittima Salangsing*[1)], *Anissa Srisongmueang*[1)], *and Santi Maensiri*[5)]

1) Department of Science and Mathematics, Faculty of Science and Health Technology, Kalasin University, Kalasin 46000, Thailand
2) The Office of Disease Prevention and Control-Region 4, Department of Disease Control, Ministry of Public Health, Saraburi 18120, Thailand
3) Synchrotron Light Research Institute (Public Organisation), Nakhon Ratchasima 30000, Thailand
4) Department of Physics, Faculty of Science, Khon Kaen University, Khon Kaen 40002, Thailand
5) School of Physics, Institute of Science, Suranaree University of Technology, Nakhon Ratchasima, 30000 Thailand
(Received: 13 May 2024; revised: 5 September 2024; accepted: 8 October 2024)

Abstract: The $Fe_{1-x}Ni_xVO_4$ (x = 0, 0.05, 0.10, and 0.20) nanoparticles in this work were successfully synthesized via a co-precipitation method. The structural, magnetic and electrochemical properties of the prepared $Fe_{1-x}Ni_xVO_4$ nanoparticles were studied as a function of Ni content. The experimental results show that the prepared Ni-doped $FeVO_4$ samples have a triclinic structure. Scanning electron microscopy (SEM) images reveal a decrease in average nanoparticle size with increasing Ni content, leading to an enhancement in both specific surface area and magnetization values. X-ray absorption near edge structure (XANES) analysis confirms the substitution of Ni^{2+} ions into Fe^{3+} sites. The magnetic investigation reveals that Ni-doped $FeVO_4$ exhibits weak ferromagnetic behavior at room temperature, in contrast to the antiferromagnetic behavior observed in the undoped $FeVO_4$. Electrochemical studies demonstrate that the $Fe_{0.95}Ni_{0.05}VO_4$ electrode achieves the highest specific capacitance of 334.05 $F\cdot g^{-1}$ at a current density of 1 $A\cdot g^{-1}$, which is attributed to its smallest average pore diameter. In addition, the enhanced specific surface of the $Fe_{0.8}Ni_{0.2}VO_4$ electrode is responsible for its outstanding cyclic stability. Overall, our results suggest that the magnetic and electrochemical properties of $FeVO_4$ nanoparticles could be effectively tuned by varying Ni doping contents.

Keywords: iron vanadate ($FeVO_4$); co-precipitation method; Ni doping content; magnetic properties; electrochemical properties

1. Introduction

In the last few decades, global energy production has seen a dramatic increase, primarily driven by industrialization and urbanization [1]. The utilization of fossil fuels for energy production has had a significant impact on the environment. The release of carbon dioxide (CO_2) during fossil fuel combustion contributes to the greenhouse effect, leading to global warming [2–3]. Consequently, alternative energy sources like solar energy, wind energy, hydropower, and biomass energy have become crucial for mitigating CO_2 emissions [4–5]. To capture and store energy produced from these sources, energy storage devices like batteries and supercapacitors are essential. Among the energy storage devices, electrochemical capacitors or supercapacitors are attracting significant attention owing to their fast charging/discharging, long cycling stability, and high-power density [6–8]. Basically, supercapacitors can be categorized into two main types based on their charge storage mechanism. An electric double layer capacitor (EDLC) stores energy through the electrostatic double-layer capacitance formed at the interface of electrode/electrolyte [9]. In contrast, pseudocapacitor stores energy through reversible Faradaic redox reactions at the electrode/electrolyte interface [10]. Therefore, materials such as transition metal oxides and conducting polymers are commonly used as electrodes in pseudocapacitors [11]. However, the electrochemical performance of pseudocapacitive materials is limited due to their low conductivity, low surface area, and poor electrochemical activity [12–13]. One efficient strategy for enhancing the electrochemical performances of these materials is to introduce metal elements, known as metal doping, into the host materials [14].

Transition metal vanadates with the general formula AVO_4 (A = Ti, Fe, In, Sm, Cr, Bi, etc) are increasingly interested in a wide range of applications [15]. For example, Sajid *et al*. [16] synthesized $BiVO_4$ by using a sonicated assisted hydrothermal method for electrochemical sensors and visible light photocatalysis. Majumder *et al*. [17] prepared $FeVO_4$ nanopebble thin film using two-step synthesis involving hydrothermal and drop casing for efficient photoelectrochemical water splitting applications. Among transition metal vanadates, iron vanadate ($FeVO_4$) has gained attention as a potential electrode material for energy storage applications,

✉ Corresponding author: Jessada Khajonrit E-mail: Ex_phys@hotmail.com

particularly in batteries and supercapacitors [18–19]. In general, $FeVO_4$ exists in four polymorphs named as $FeVO_4$-I, $FeVO_4$-II, $FeVO_4$-III, and $FeVO_4$-IV. At room temperature, the stable phase of $FeVO_4$-I possesses a triclinic structure [20]. While the metastable phases under high pressure and high temperature of $FeVO_4$-II and $FeVO_4$-III have orthorhombic structure, whereas $FeVO_4$-IV is usually formed monoclinic structure [21]. Such various structures of $FeVO_4$ are of interest in different applications such as photoanode in water splitting [22], catalyst [23], electrochemical sensor [24], and energy storage [19]. In the $FeVO_4$-I structure, the Fe^{3+} ions have three crystallographic sites in which two sites are in distorted octahedral FeO_6 and one site is in the distorted trigonal bipyramidal FeO_5 environment [25]. A six-column doubly bent chain via edge-sharing of Fe–O polyhedra is formed and the chains are linked together by VO_4 tetrahedra, forming a three-dimensional framework [25]. Regarding its crystal structure, $FeVO_4$ is selected as the electrode material for the supercapacitor due to the presence of multiple oxidation states of Fe^{3+} and V^{5+}. Besides its advantages, $FeVO_4$ still faces serious problems for achieving high electrochemical performance such as rapid capacity decay and low electronic conductivity [26]. These problems can impact the overall electrochemical performance of $FeVO_4$-based energy storage devices. Several strategies such as nanostructuring and doping have been adopted to address these issues. Recently, the preparation of $FeVO_4$ nanostructure using sol–gel auto-combustion technique and its enhanced electrochemical performance was reported [27]. Otherwise, one of the common strategies used to increase the electrical properties of materials is the addition or doping a small percentage of foreign atoms in the regular crystal lattice [28–29]. In this regard, Munir Sajid *et al*. [30] synthesized Bi-doped $FeVO_4$ by using a hydrothermal method and the improved conductivity was observed due to the hopping of electrons between Bi and Fe ions. The improved charge carrier transport and conductivity through Ni doping in α-Fe_2O_3 owing to the occupied Ni atoms in the lattice positions of Fe atoms were reported [31]. Therefore, the replacement of Ni in lattice positions of Fe atoms might efficiently tune their electronic structure and intrinsic properties, significantly affecting chemical reactions taking place at the interfaces, resulting in high electrochemical performance of $FeVO_4$ [32]. To the best of our knowledge, there is no report on the electrochemical characteristics of Ni-doped $FeVO_4$ for supercapacitor applications. The existing studies focus on the use of Ni in $FeVO_4/TiO_2$ monolith catalysts for selective catalytic reduction reactions [33], as well as research on the effect of Ni addition on the electrochemical performance of $FeVO_4$ in water separation applications [34].

In this study, Ni-doped $FeVO_4$ with varying Ni contents was prepared by using a co-precipitation method. The effects of Ni doping contents were deepened the understanding on the structural, morphological, and electrochemical characteristics of $FeVO_4$. The results demonstrated that Ni doping improved the magnetic and electrochemical properties of $FeVO_4$. An increase in Ni content resulted in an increase in specific surface area and thus enhancing the magnetization values and electrochemical performances of $FeVO_4$. Consequently, the Ni-doped $FeVO_4$ nanoparticles could be considered as excellent electrode materials for energy storage devices.

2. Experimental

2.1. Preparation of $Fe_{1-x}Ni_xVO_4$ nanostructure

The $Fe_{1-x}Ni_xVO_4$ nanoparticles (x = 0, 0.05, 0.10, and 0.20) were prepared by using a modified co-precipitation method by mixing iron (III) nitrate nonahydrate ($Fe(NO_3)_3 \cdot 9H_2O$), nickel (II) nitrate hexahydrate ($Ni(NO_3)_2 \cdot 6H_2O$), and ammonium metavanadate (NH_4VO_3) in deionized water and stirring for 1 h. Then, sodium hydroxide (NaOH) was added, followed by stirring for 1 h. The precipitate was washed with deionized water 5 times and then dried in an oven at 60°C for 24 h. The prepared $Fe_{1-x}Ni_xVO_4$ samples were calcined at a temperature of 600°C for 3 h.

2.2. Materials characterizations

The crystal structure of the prepared $FeVO_4$ nanoparticles was characterized by using X-ray diffraction (XRD; D2 Phaser), The effect of Ni doping contents on the morphology of the prepared $FeVO_4$ was revealed by using scanning electron microscopy (SEM; JSM-7800F). The oxidation states of Ni, Fe, and V at K-edges were examined by using X-ray absorption near edge spectra (XANES) in transmission mode at the Synchrotron Light Research Institute (BL5.2), Nakhon Ratchasima, Thailand. The obtained XANES spectra were normalized by using ATHENA software [35]. The specific surface area (SSA) and porosity of the prepared Ni-doped $FeVO_4$ were carried out by using the N_2 adsorption/desorption technique (BELSORP-miniII instruments). Before the measurements, all samples were thoroughly degassed at 80°C for 18 h. The specific surface area (S_{BET}), mean pore diameter (D_{MP}), and total pore volume (V_{TP}) were investigated using the Brunauer–Emmett–Teller (BET) method. In addition, the magnetic properties of the prepared Ni-doped $FeVO_4$ were conducted using a vibrating sample magnetometer (VSM) at room temperature over a magnetic field range of ±30 kOe.

2.3. Electrochemical measurement

The electrochemical properties of the prepared $Fe_{1-x}Ni_xVO_4$ electrodes were studied in 3 $mol \cdot L^{-1}$ KOH aqueous electrolyte by using a three-electrode system consisting of working electrode, counter electrode, and reference electrode. Working electrode was fabricated by mixing the Ni-doped $FeVPO_4$ nanoparticles (80wt%), acetylene black (10wt%), and a binder of polyvinylidene difluoride (10wt%) using n-methyl-2-pyrrolidinone (NMP) as a solvent. The obtained slurry was coated on a nickel foam current collector and dried at 70°C for 12 h. Before the electrochemical measurements, the dried electrodes were pressed at 2 MPa and soaked in the aqueous electrolyte overnight. Two well-known techniques consisting of cyclic voltammetry (CV) and galvanostatic charge–discharge (GCD) were performed to as-

sess the electrochemical performances of the prepared electrodes.

3. Results and discussion

3.1. Structural and morphological analysis

Fig. 1(a) shows the XRD patterns of the prepared $Ni_xFe_{1-x}VO_4$ (x = 0, 0.05, 0.10, 0.20). The diffraction peaks were indexed as triclinic structure of $FeVO_4$ (JCPDS No.00-038-1372) in all samples, except for those with x = 0.05 sample, which indicated the structure of $FeVO_4$ (JCPDS No.01-071-1592) with space group of $P\bar{1}$ indicating the successfully prepared Ni-doped $FeVO_4$ using a co-precipitation method. This is in accordance with the previous literature [36]. The main XRD patterns indicate that as the Ni doping content increases, there is a noticeable decrease in the intensity of the peaks. According to the Scherrer equation, the decrease in crystallite size causes the XRD peaks to broaden [37]. Therefore, the decreasing peak intensities suggest the decrease in crystallite size after Ni doping. Clearly, the XRD peak at $2\theta \approx 25°$ of x = 0.05 in Fig. 1(b) shifts toward a higher diffraction angle without formation of the secondary phase. This is caused by the substitution of the very close ionic radii of Fe^{3+} (0.65 Å) [38] with the Ni^{2+} (0.69 Å) [39].

To give the important information regarding to shape and size of the prepared materials, the morphologies of the prepared Ni-doped $FeVO_4$ using a co-precipitation method at different Ni doping contents of x = 0, 0.05, 0.10, and 0.20 were revealed by SEM images and shown in Fig. 2. It is evident that the nearly spherical shapes of the $FeVO_4$ are well connected with the others, forming a network. The determination of particle size using Image J software found that the average diameters of the nearly spherical particles are of 109.8 ± 23.0, 105.1 ± 22.7, 90.7 ± 18.4, and 89.7 ± 9 nm for x = 0, 0.05, 0.10, and 0.20, respectively. Hence, the addition of Ni dopant plays an important role in the reduction of particle size in which the particle size decreased with increasing Ni doping contents. In general, the smaller particle sizes offer

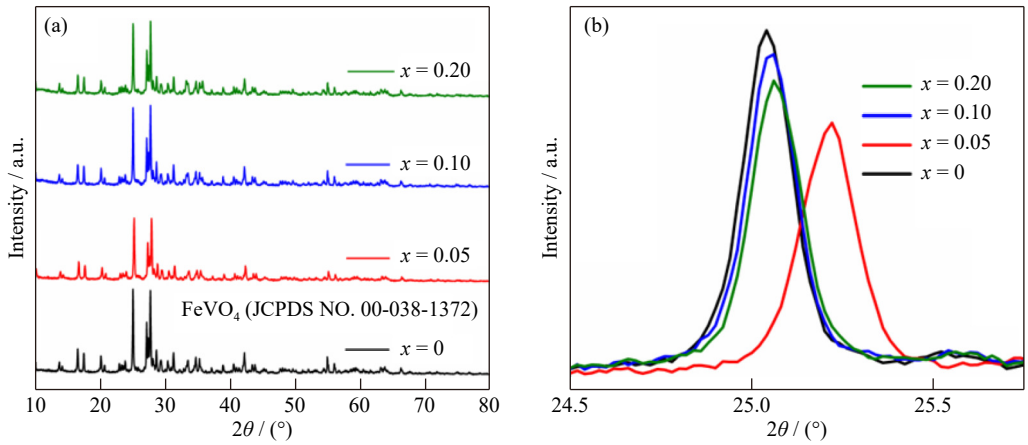

Fig. 1. (a) Full XRD patterns of the $Fe_{1-x}Ni_xVO_4$ (x = 0, 0.05, 0.10, and 0.20) and (b) magnified XRD patterns of these samples within a 2θ range from 24.5° –26.0°.

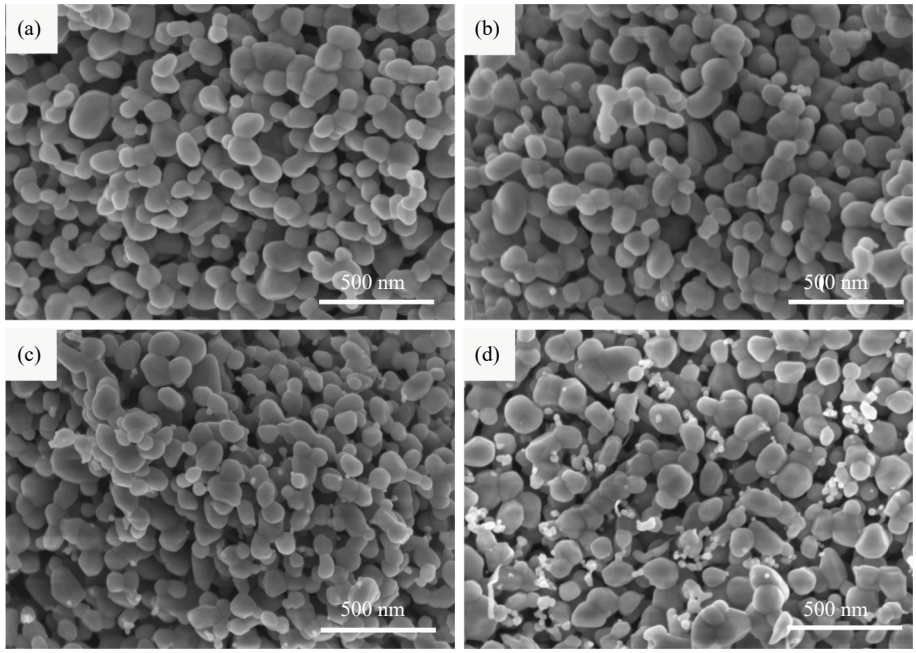

Fig. 2. SEM images of the prepared $Fe_{1-x}Ni_xVO_4$ nanoparticles: (a) x = 0, (b) x = 0.05, (c) x = 0.10, and (d) x = 0.20.

higher surface-to-volume ratio, which lead to an enhancement of electronic conductivity. This could turn to improve the electrochemical performance of the materials after Ni doping. In the field of energy storage, smaller particle sizes could provide more active sites for Faradaic redox reaction, thereby enhancing electrochemical performance [40]. It is interesting that as the Ni doping content is increased the addition of the smaller secondary particle sizes is more presented. Therefore, the doping of Ni causes the additional secondary particles. This could affect magnetic and electrochemical properties of the prepared materials.

To examine the oxidation states of Ni, Fe, and V in the prepared materials, the XANES technique was carried out. Fig. 3 presents normalized XANES spectra of the prepared Ni-doped $FeVO_4$ at (a) Ni, (b) Fe, and (c) V K-edges, respectively. The XANES spectra of the prepared samples were compared with the reference standards of Ni foil (Ni^0), $Ni(OH)_2$ (Ni^{2+}), NiO (Ni^{2+}), Fe foil (Fe^0), FeO (Fe^{2+}), Fe_2O_3 (Fe^{3+}), V_2O_3 (V^{3+}), VO_2(V^{4+}), and V_2O_5 (V^{5+}). As a result, the absorption edges of the prepared $Fe_{1-x}Ni_xVO_4$ at Ni K-edge match well with the absorption edge of $Ni(OH)_2$ standard sample. This indicates the oxidation state of Ni is +2. In case of Fe K-edge, the absorption edges of the prepared $Fe_{1-x}Ni_xVO_4$ are close to those of Fe_2O_3. This signifies the presence of Fe^{3+} ions in the crystal structure of the prepared materials. In Fig. 4(c), the XANES spectra are similar to those of the V_2O_5 which indicates a +5 oxidation state of V ions. Overall, XANES results strongly suggest that Ni^{2+}

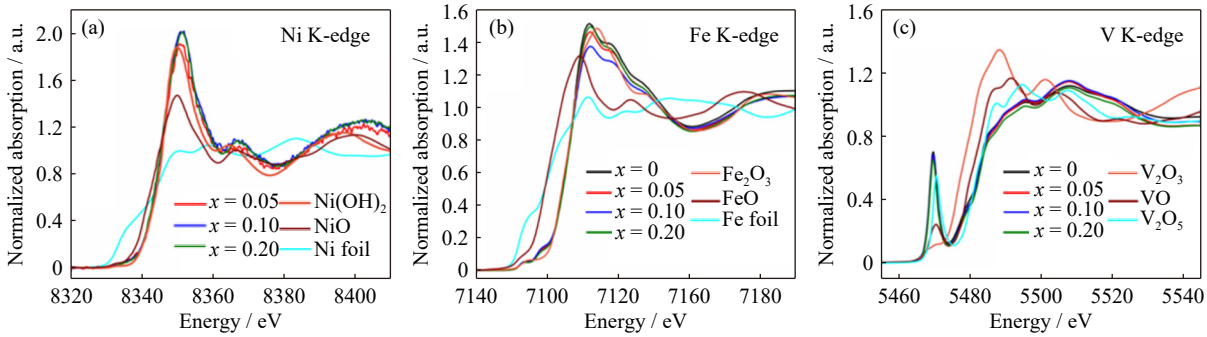

Fig. 3. XANES spectra of the prepared $Fe_{1-x}Ni_xVO_4$ nanoparticles at (a) Ni K-edge, (b) Fe K-edge, and (c) V K-edge.

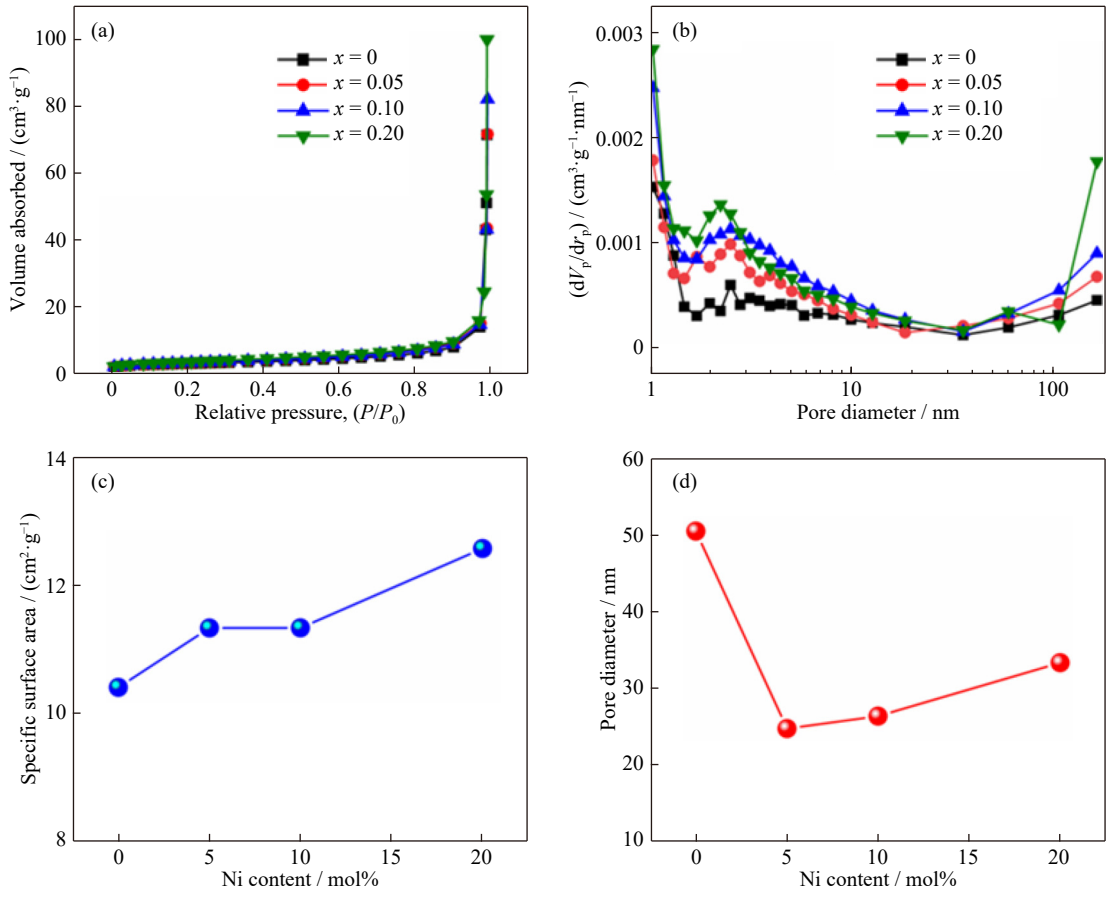

Fig. 4. (a) N_2 adsorption–desorption isotherms, (b) BJH pore size distribution, (c) BET specific surface area (S_{BET}), and (d) BET pore diameter (D_{BET}) versus Ni contents of the prepared Ni-doped $FeVO_4$ nanoparticles. P, P_0, V_p, and r_p are the absolute gas pressure, saturation pressure, pore volume, and pore radius, respectively.

(0.69 Å) substitutes the Fe^{3+} (0.65 Å) site. The edge energy and oxidation state of the standard samples and the $Fe_{1-x}Ni_xVO_4$ nanoparticles are shown in Table 1. The increase in Ni content leads to a slight decrease in edge energies (8346.20, 8345.80, and 8345.26 eV for the Ni K-edge and 7127.18, 7126.75, and 7126.66 eV for the Fe K-edge) for x = 0.05, 0.10, and 0.20 samples, respectively. The decreasing in the edge energies of Ni K-edge and Fe K-edge for x = 0.05, 0.10, and 0.20 samples correspond to a decrease in particle size of the $Fe_{1-x}Ni_xVO_4$ nanoparticles. Interestingly, the highest edge energies of the Ni K-edge for the x = 0.05 sample confirm the substitution at the Fe site and phase transformation, which may affect the electrochemical performance values.

Table 1. Edge energy and oxidation state of the standard samples and the prepared $Fe_{1-x}Ni_xVO_4$ nanoparticles

Sample	Edge element	Absorption edge / eV	Oxidation state
Ni foil	Ni	8333.23	0
$Ni(OH)_2$	Ni	8346.56	+2
NiO	Ni	8343.74	+2
Fe foil	Fe	7112.12	0
FeO	Fe	7120.86	+2
Fe_2O_3	Fe	7125.90	+3
$FeVO_4$	Fe	7126.70	+3
$Fe_{0.95}Ni_{0.05}VO_4$	Ni	8346.20	+2
	Fe	7127.18	+3
$Fe_{0.9}Ni_{0.1}VO_4$	Ni	8345.80	+2
	Fe	7126.75	+3
$Fe_{0.8}Ni_{0.2}VO_4$	Ni	8345.26	+2
	Fe	7126.66	+3

3.2. Porous structure analysis

It is well known that the specific surface area, pore size, and pore volume influence the electrochemical performances of the electroactive materials. Fig. 4(a) shows the N_2 adsorption/desorption isotherms of the prepared $Fe_{1-x}Ni_xVO_4$ samples. According to the International Union of Pure and Applied Chemistry (IUPAC) classification, the isotherms with a hysteresis loop exhibit a typical type IV, indicating the existence of mesopores in our prepared materials. The calculated specific surface area (S_{BET}) using a Brunauer–Emmett–Teller method as summarized in Table 2 slightly increases from 10.405 to 12.574 $m^2 \cdot g^{-1}$ with increasing Ni doping contents up to 20mol%. This could be explained owing to the reduction of particle sizes after Ni doping as observed in SEM images. Notably, the results confirm that Ni doping is beneficial for increasing the specific surface area of $FeVO_4$.

Fig. 4(b) shows the Barrett–Joyner–Halenda (BJH) pore size distribution of the prepared $Fe_{1-x}Ni_xVO_4$ samples. It is evident that the pore diameters of all samples are centered at about 2–3 nm, confirming the mesoporous nature in the prepared materials. The average BJH pore diameter (D_{BJH}) as summarized in Table 2 shows the decrease after Ni doping. The $Fe_{0.95}Ni_{0.05}VO_4$ sample represents the smallest pore diameter of 19.846 nm. The smaller pore size suggests the higher specific capacitance value due to the electrolyte ions are more easily accessible to the electroactive materials [41]. Hence, the sample of $Fe_{0.95}Ni_{0.05}VO_4$ is expected to provide the highest specific capacitance value in comparison with others.

Table 2. BET specific surface area (S_{BET}) and average BJH pore diameter (D_{BJH}) calculated by N_2 adsorption/desorption measurements, as well as specific capacitances obtained by CV and GCD measurements for different samples

Sample	S_{BET} / ($m^2 \cdot g^{-1}$)	D_{BJH} / nm	Specific capacitance / ($F \cdot g^{-1}$)	
			CV (at 5 $mV \cdot s^{-1}$)	GCD (at 1 $A \cdot g^{-1}$)
$FeVO_4$	10.405	45.998	101.19	70.19
$Fe_{0.95}Ni_{0.05}VO_4$	11.333	19.846	141.67	334.05
$Fe_{0.9}Ni_{0.1}VO_4$	11.335	33.538	136.72	325.02
$Fe_{0.8}Ni_{0.2}VO_4$	12.574	32.445	116.26	99.57

3.3. Magnetic study

The magnetization curves of the prepared $Fe_{1-x}Ni_xVO_4$ nanoparticles (x = 0, 0.05, 0.10, and 0.20) obtained from VSM measurements at room temperature are presented in Fig. 5. Clearly, all doped samples exhibit hysteresis loops in the field range of ±30 kOe, indicating a weak ferromagnetism. Whereas the antiferromagnetic is presented in the undoped sample. This is in good agreement with the literature [19,25]. Obviously, the magnetization values of 2.26, 2.52, and 3.58 $emu \cdot g^{-1}$ were observed for the samples of x = 0.05, 0.10, and 0.20, respectively. It is well-known that the magnetization of the material is defined as the degree of alignment of magnetic dipoles for a given applied magnetic field [42]. Therefore, the higher magnetization values might be explained due to the well aligned magnetic dipoles and thus enhancing magnetic interactions between particles in smaller particle size providing larger specific surface area after increasing Ni doping contents [43]. Therefore, our results suggest that the particle size and specific surface area of $FeVO_4$ can influence the magnetization of the nanoparticles.

3.4. Electrochemical study

Fig. 6 depicts the CV curves of the prepared Ni-doped $FeVO_4$ electrodes with different Ni doping contents over the potential window range of −1.2 to 0 V. Clearly, the CV curves of all samples show broad peaks exhibiting pseudocapacitive behavior. The broad peaks might be due to the overlapping at the near potential of the Fe^{3+}/Fe^{2+} and V^{5+}/V^{4+} redox couples [44–45]. As presented in the figure, the en-

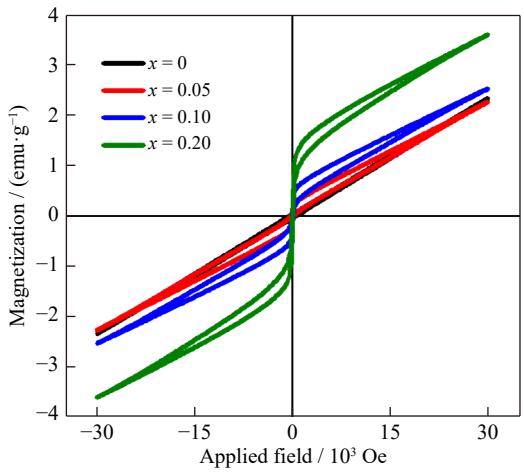

Fig. 5. Magnetization as a function of the magnetic field of the prepared $Fe_{1-x}Ni_xVO_4$ nanoparticles measured in the field range of ±30 kOe at room temperature.

hanced response currents and the progressive shifts of redox peaks with increasing scan rates are observed. This implies that the capacitance originates from the redox reactions [46]. In addition, the increased current values and area under CV curves after Ni doping suggest the higher specific capacitance value in these electrodes. Compared with Ni doping contents, the increase in Ni content leads to a decrease in the area under CV curves, implying the decrease in the specific capacitance value. The shifts of oxidation and reduction peaks while increasing scan rates are possibly caused by a polarization effect because of the increasing Ni content [47].

The GCD curves at various current densities of 1–20 $A \cdot g^{-1}$ of the prepared Ni-doped $FeVO_4$ electrodes are shown in Fig. 7. Obviously, the non-symmetric shapes of all prepared electrodes indicate a pseudocapacitive behavior. As shown in Fig. 7, the Ni-doped $FeVO_4$ electrodes has much longer discharging time than that of the undoped electrodes, implying that the doped samples have higher specific capacitance values. In comparison with those of the Ni doping contents, the longest discharging time is observed in the sample of x = 0.05, followed by x = 0.10 and 0.20, respectively.

Fig. 8 displays the specific capacitance as a function of scan rates and current densities of the prepared Ni-doped $FeVO_4$ electrodes, which were calculated from the equations [48–49]. It is observed that the specific capacitance of the electrode decreases with an increasing scan rate. This could be explained because the electrolyte ions do not have enough time to diffuse deep into pores of the electrode materials at higher scan rates, while the electrolyte ions have enough time to arrive at the pores of the electrode at low scan rates [50]. Similarly, the specific capacitances calculated from the CV and GCD curves of the electrode increase in the electrode at x = 0.05 first and then decrease after continuously increasing Ni doping contents. The increasing specific capacitance value could be explained due to the reduction of particle size, which provides more redox sites after Ni doping. On the other hand, the decrease in capacitance value after increasing Ni doping contents from 5mol% to 20mol% is due to the en-

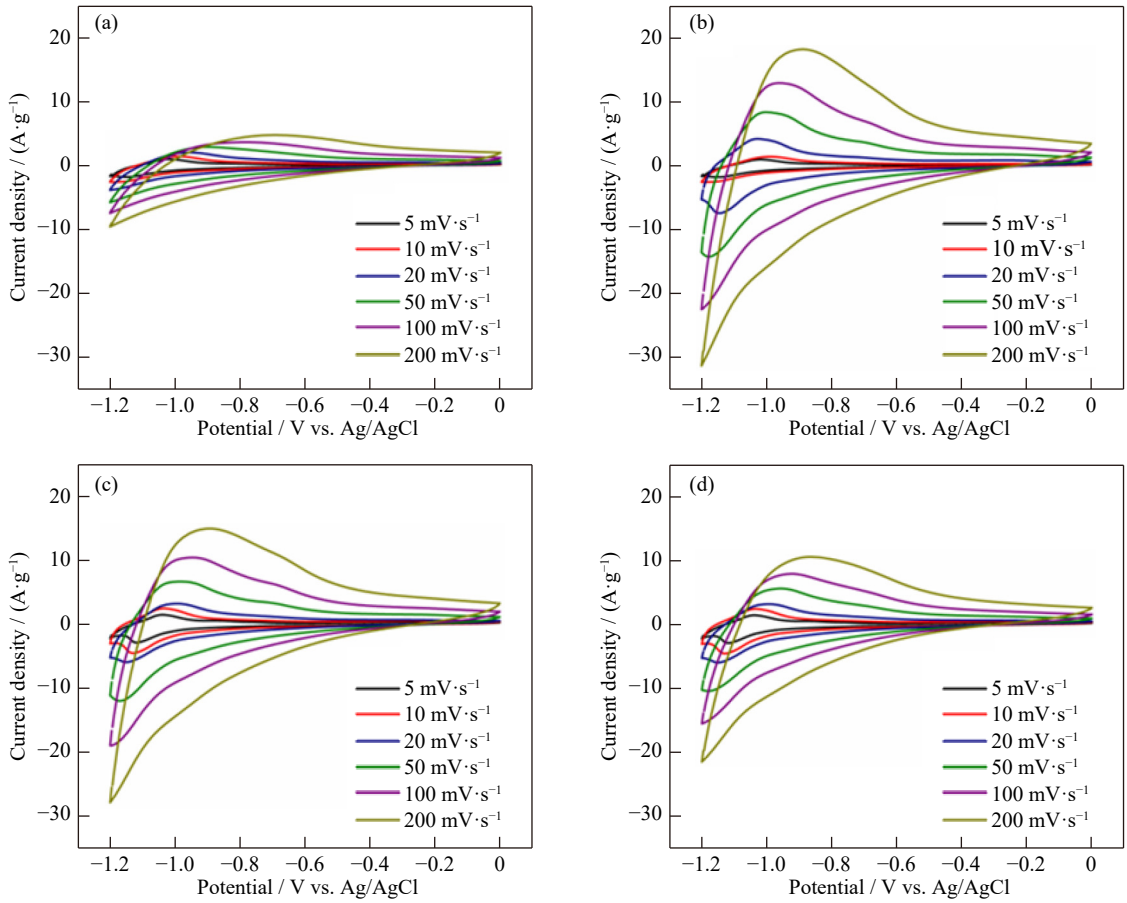

Fig. 6. Cyclic voltammetry (CV) curves of the prepared $Fe_{1-x}Ni_xVO_4$ electrodes: (a) x = 0, (b) x = 0.05, (c) x = 0.10, and (d) x = 0.20.

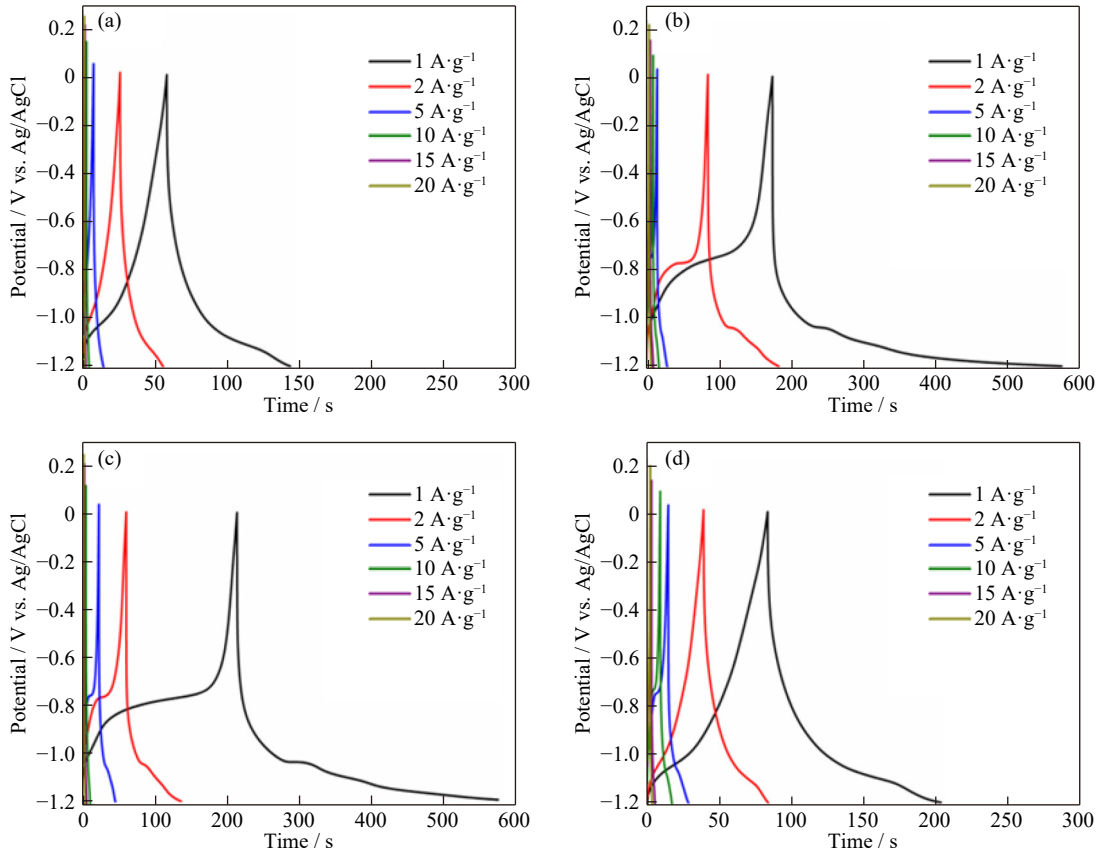

Fig. 7. Galvanostatic charge–discharge (GCD) curves of the $Fe_{1-x}Ni_xVO_4$ electrodes: (a) x = 0, (b) x = 0.05, (c) x = 0.10, and (d) x = 0.20.

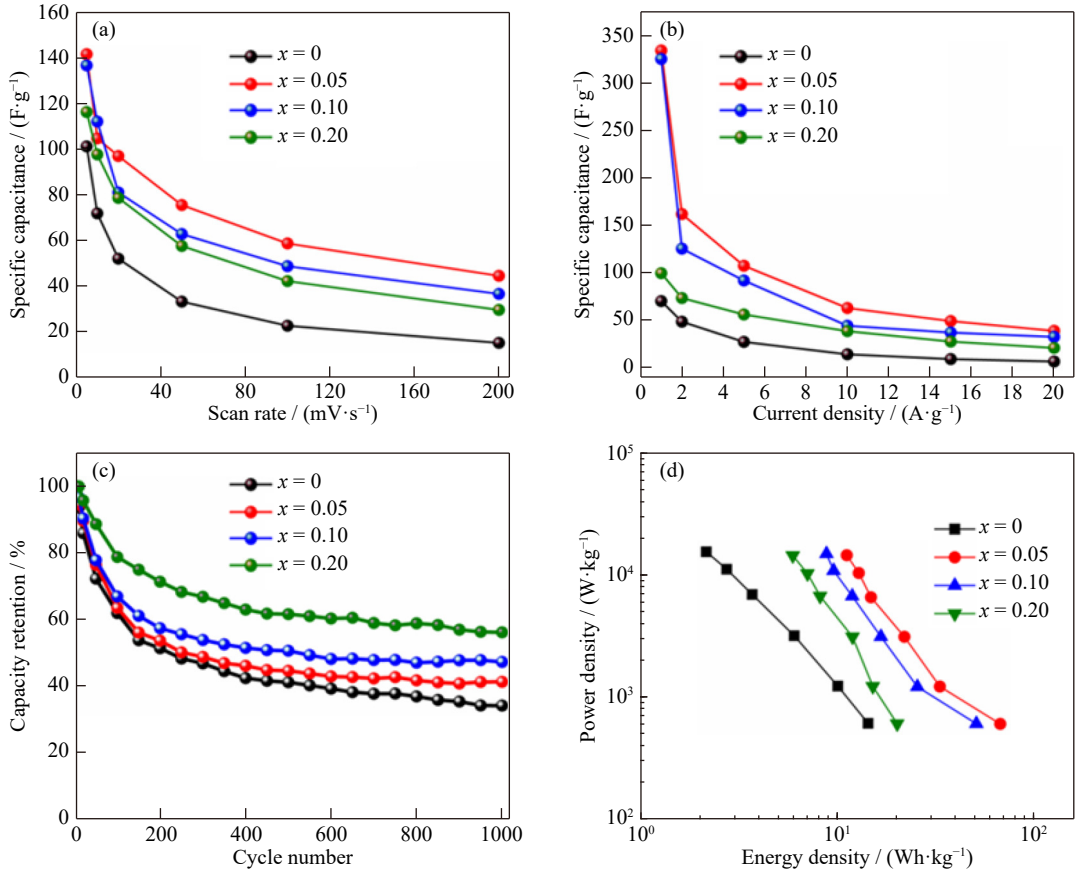

Fig. 8. Specific capacitance as a function of (a) scan rate, (b) current density, (c) the cyclic stability, and (d) energy versus power densities of the $Fe_{1-x}Ni_xVO_4$ electrodes.

hanced average BJH pore diameter (D_{BJH}) from 19.846 to 32.445 nm. As summarized in Table 2, the 5mol% Ni-doped $FeVO_4$ electrode exhibits the maximum specific capacitance values of 141.67 and 334.05 $F \cdot g^{-1}$ at a scan rate of 5 $mV \cdot s^{-1}$ and a current density of 1 $A \cdot g^{-1}$, respectively. This is due to the increased surface area of the smaller average mesopore size. To compare our electrochemical result with other reports, Table 3 summarizes the specific capacitance value of $FeVO_4$-based materials prepared using different methods. As a result, a simple preparation using co-precipitation method provides the higher specific capacitance value in comparison with the similar morphology of spherical shape.

For the long-term study, all electrodes were charged and discharged at a current density of 10 $A \cdot g^{-1}$ for 1000 cycles. As a result, the specific capacitance values of the Ni-doped $FeVO_4$ electrodes with x = 0, 0.05, 0.10 and 0.20 after 1000 cycles retained 34.18%, 41.29%, 47.26%, and 56.15%, respectively (Fig. 8(c)). The larger specific surface area, which provides more active sites, is responsible for the outstanding cyclic stability of the $Fe_{0.8}Ni_{0.2}VO_4$ electrode. For practical applications, energy density and power density are the important performance parameters. The energy density and power density were calculated by the equations [54] and shown in Fig. 8(d). As a result, the energy densities were calculated to be 66.98, 50.68, 20.12, and 14.33 $Wh \cdot kg^{-1}$ and the power densities of 600.75, 603.10, 603.10, and 606.30 $W \cdot kg^{-1}$ for x = 0.05, 0.10, 0.20, and 0,respectively, at a current density of 1 $A \cdot g^{-1}$. The improving energy density of the x = 0.05 sample is about 3.7 time higher than that of the undoped $FeVO_4$ sample. The achieved highest energy density could be explained owing to the smallest average mesopore size in this sample. Therefore, Ni-doped $FeVO_4$ could be effectively used as electrode materials for supercapacitors.

Table 3. Comparison of the specific capacitance of the prepared $FeVO_4$-based materials using various methods with other reports

Preparation method	Morphology	Particle size	Specific capacitance	Ref.
Wet chemical synthesis	Polyhedron shape	~200 nm	402 $F \cdot g^{-1}$ at 10 $mV \cdot s^{-1}$	[19]
Sol–gel auto-combustion	Nanoparticles		1151.05 $F \cdot g^{-1}$ at 5 $mV \cdot s^{-1}$	[27]
Co-precipitation	Spherical particles	30–40 nm	97.54 $F \cdot g^{-1}$ at 0.5$mA \cdot cm^{-2}$	[51]
Co-precipitation	Polyhedron shape	100–200 nm	376 $F \cdot g^{-1}$ at 20 $mV \cdot s^{-1}$	[52]
Surfactant-assisted hydrothermal	Nanoparticles		48 $F \cdot g^{-1}$	[53]
Co-precipitation	Spherical particles	80–110 nm	334.05 $F \cdot g^{-1}$ at 1 $A \cdot g^{-1}$	This work

4. Conclusion

In this work, the $Fe_{1-x}Ni_xVO_4$ (x = 0, 0.05, 0.10, and 0.20) nanoparticles were successfully synthesized via a co-precipitation method. The influence of varying Ni doping contents on the structural, magnetic, and electrochemical properties of $FeVO_4$ nanoparticles were studied. Experimental results indicate that the obtained Ni-doped $FeVO_4$ nanoparticles exhibit a triclinic structure. An observed decrease in nanoparticle size with increasing Ni content leads to an increase in BET surface area, rising from 10.405 to 12.574 $m^2 \cdot g^{-1}$. The smallest average BJH pore size is found to be 19.846 nm, which in turn delivers the highest specific capacitance value in the $Fe_{0.95}Ni_{0.05}VO_4$ electrode. XANES analysis reveals that the oxidation states of Ni, Fe, and V ions in the Ni-doped $FeVO_4$ structure are +2, +3, and +5, respectively. The magnetic properties turn from antiferromagnetic to ferromagnetic after Ni doping and the magnetization values increase with increasing Ni doping contents. This is attributed to the reduction of particle size. The $Fe_{0.95}Ni_{0.05}VO_4$ electrode exhibits the highest specific capacitance value of 334.05 $F \cdot g^{-1}$ at a current density of 1 $A \cdot g^{-1}$, which is explained by the smallest average pore size. Conversely, the larger specific surface area of the $Fe_{0.8}Ni_{0.2}VO_4$ electrode contributes to its excellent long-term cycling stability. Hence, doping with varying Ni content could adjust the structure, magnetic and electrochemical properties of $FeVO_4$.

Acknowledgements

The author would like to thank (1) Materials Innovation (MI) group, Department of Science and Mathematics, Faculty of Science and Health Technology, Kalasin University, Kalasin, Thailand; (2) The Advanced Materials Physics (AMP) group, Suranaree University of Technology, Nakhon Ratchasima, Thailand for the facility of electrochemical measurements; (3) The Synchrotron Light Research Institute (BL5.2 XAS), Nakhon Ratchasima, Thailand; and (4) the Department of Physics, Faculty of Science, Khon Kaen University, Khon Kaen, Thailand for VSM facilities.

Conflict of Interest

All authors do not have competing interests to declare.

References

[1] D.J. Pandya, P. Muthu Pandian, I. Kumar, *et al*., Supercapacitors: Review of materials and fabrication methods, *Mater. Today Proc*., (2023) DOI: 10.1016/j.matpr.2023.10.148.

[2] T.R. Anderson, E. Hawkins, and P.D. Jones, CO_2, the greenhouse effect and global warming: From the pioneering work of Arrhenius and Callendar to today's Earth System Models, *Endeavour*, 40(2016), No. 3, p. 178.

[3] K.O. Yoro and M.O. Daramola, CO_2 emission sources, greenhouse gases, and the global warming effect, [in] M.R. Rahimpour, M. Farsi and M.A. Makarem, *Advances in Carbon Capture*, Woodhead Publishing, Cambridge, 2020, p. 3.

[4] T.Z. Ang, M. Salem, M. Kamarol, H.S. Das, M.A. Nazari, and N. Prabaharan, A comprehensive study of renewable energy sources: Classifications, challenges and suggestions, *Energy Strategy Rev.*, 43(2022), art. No. 100939.
[5] E. Gul, G. Baldinelli, P. Bartocci, *et al*., Transition toward net zero emissions - Integration and optimization of renewable energy sources: Solar, hydro, and biomass with the local grid station in central Italy, *Renewable Energy*, 207(2023), p. 672.
[6] P. Simon and Y. Gogotsi, Materials for electrochemical capacitors, *Nat. Mater.*, 7(2008), No. 11, p. 845.
[7] Y.L. Shao, M.F. El-Kady, J.Y. Sun, *et al*., Design and mechanisms of asymmetric supercapacitors, *Chem. Rev.*, 118(2018), No. 18, p. 9233.
[8] P.H. Yang and W.J. Mai, Flexible solid-state electrochemical supercapacitors, *Nano Energy*, 8(2014), p. 274.
[9] S.H. Chen, L. Qiu, and H.M. Cheng, Carbon-based fibers for advanced electrochemical energy storage devices, *Chem. Rev.*, 120(2020), No. 5, p. 2811.
[10] X.Y. Lang, A. Hirata, T. Fujita, and M.W. Chen, Nanoporous metal/oxide hybrid electrodes for electrochemical supercapacitors, *Nat. Nanotechnol.*, 6(2011), No. 4, p. 232.
[11] C. Choi, D.S. Ashby, D.M. Butts, *et al*., Achieving high energy density and high power density with pseudocapacitive materials, *Nat. Rev. Mater.*, 5(2020), No. 1, p. 5.
[12] R.B. Liang, Y.Q. Du, P. Xiao, *et al*., Transition metal oxide electrode materials for supercapacitors: A review of recent developments, *Nanomaterials*, 11(2021), No. 5, art. No. 1248.
[13] H.W. Park and K.C. Roh, Recent advances in and perspectives on pseudocapacitive materials for supercapacitors–A review, *J. Power Sources*, 557(2023), art. No. 232558.
[14] D.B. Malavekar, V.V. Magdum, S.D. Khot, J.H. Kim, and C.D. Lokhande, Doping of rare earth elements: Towards enhancing the electrochemical performance of pseudocapacitive materials, *J. Alloys Compd.*, 960(2023), art. No. 170601.
[15] A. Alsulami, Y.K. Kumarswamy, M.K. Prashanth, *et al*., Fabrication of $FeVO_4$/RGO nanocomposite: An amperometric probe for sensitive detection of methyl parathion in green beans and solar light-induced degradation, *ACS Omega*, 7(2022), No. 49, p. 45239.
[16] M.M. Sajid, H.F. Zhai, M.A. Iqbal, N.A. Shad, and A. Munawar, Tunable Fe^{+3} and W^{+6} Co-doped BiVO4 nanohybrids with efficient photocatalytic and electrochemical chemical sensing characteristics, *Ceram. Int.*, 50(2024), No. 1, p. 957.
[17] S. Majumder, A.A. Yadav, L.A.M. Gomez, Y.M. Hunge, R. Srinivasan, and K.H. Kim, Unlocking clean energy: Exploring $FeVO_4$ nanopebble thin film as an outstanding photoanode for efficient water splitting, *J. Alloys Compd.*, 1002(2024), art. No. 175391.
[18] X.G. Niu, Y.C. Zhang, L.L. Tan, *et al*., Amorphous $FeVO_4$ as a promising anode material for potassium-ion batteries, *Energy Storage Mater.*, 22(2019), p. 160.
[19] M.A. Awad, A.A. Hendi, S. Natarajan, *et al*., Wet chemical synthesis and characterization of $FeVO_4$ nanoparticles for super capacitor as energy storage device, *J. King Saud Univ. Sci.*, 35(2023), No. 8, art. No. 102857.
[20] A. Dixit, G. Lawes, and A.B. Harris, Magnetic structure and magnetoelectric coupling in bulk and thin film $FeVO_4$, *Phys. Rev. B: Condens. Matter*, 82(2010), No. 2, art. No. 024430.
[21] S. López-Moreno, D. Errandonea, J. Pellicer-Porres, *et al*., Stability of $FeVO_4$ under pressure: An X-ray diffraction and first-principles study, *Inorg. Chem.*, 57(2018), No. 13, p. 7860.
[22] T.H. Nguyen, M.G. Ahmed, M.Y. Zhang, *et al*., Enhancing photoelectrochemical performance of the printed nanoporous $FeVO_4$ photoanode by dual-layer CoO_x–CoPi catalysts, *ACS Appl. Energy Mater.*, 6(2023), No. 15, p. 8297.
[23] J.Y. Feng, Z.Q. Wang, X. Zhao, *et al*., Probing the performance limitations in thin-film $FeVO_4$ photoanodes for solar water splitting, *J. Phys. Chem. C*, 122(2018), No. 18, p. 9773.
[24] U. Rajaji, Y.K. K, S.M. Chen, *et al*., Deep eutectic solvent synthesis of iron vanadate-decorated sulfur-doped carbon nanofiber nanocomposite: Electrochemical sensing tool for doxorubicin, *Mikrochim. Acta*, 188(2021), No. 9, art. No. 303.
[25] Z.Z. He, J.I. Yamaura, and Y. Ueda, Flux growth and magnetic properties of $FeVO_4$ single crystals, *J. Solid State Chem.*, 181(2008), No. 9, p. 2346.
[26] H.J. Xu, J.X. Fan, D. Pang, *et al*., Synergy of ferric vanadate and MXene for high performance Li- and Na-ion batteries, *Chem. Eng. J.*, 436(2022), art. No. 135012.
[27] O.M. Pardeshi, S. Naeem, and A.V. Patil, Synthesis of $FeVO_4$ nanoparticles using sol–gel auto-combustion method and their application in supercapacitors, *Energy Storage*, 6(2024), No. 5, art. No. e683.
[28] W.J. Jo, J.W. Jang, K.J. Kong, *et al*., Phosphate doping into monoclinic $BiVO_4$ for enhanced photoelectrochemical water oxidation activity, *Angew. Chem. Int. Ed*, 51(2012), No. 13, p. 3147.
[29] Q. Liu, B. Yang, J.Y. Liu, *et al*., Application of chemical doping and architectural design principles to fabricate nanowire $Co_2Ni_3ZnO_8$ arrays for aqueous asymmetric supercapacitors, *ACS Appl. Mater. Interfaces*, 8(2016), No. 31, p. 20157.
[30] M. Munir Sajid, H.F. Zhai, M.A. Iqbal, *et al*., Experimental insights on the synthesis and characteristics of $Fe_{1-x}Bi_xVO_4$ photocatalysts for efficient environmental and electrical applications, *Arabian J. Chem.*, 16(2023), No. 8, art. No. 104986.
[31] Y.W. Phuan, E. Ibrahim, M.N. Chong, *et al*., *In situ* Ni-doping during cathodic electrodeposition of hematite for excellent photoelectrochemical performance of nanostructured nickel oxide-hematite p–n junction photoanode, *Appl. Surf. Sci.*, 392(2017), p. 144.
[32] R. Kumar, S. Sahoo, E. Joanni, *et al*., Heteroatom doped graphene engineering for energy storage and conversion, *Mater. Today*, 39(2020), p. 47.
[33] B. Jansi Rani, G. Ravi, R. Yuvakkumar, *et al*., Ni supported anorthic phase $FeVO_4$ nanorods for electrochemical water oxidation, *Mater. Lett.*, 275(2020), art. No. 128091.
[34] G.X. Wu, X. Feng, H.L. Zhang, *et al*., The promotional role of Ni in $FeVO_4/TiO_2$ monolith catalyst for selective catalytic reduction of NO_x with NH_3, *Appl. Surf. Sci.*, 427(2018), p. 24.
[35] B. Ravel and M. Newville, *ATHENA*, *ARTEMIS*, *HEPHAESTUS*: Data analysis for X-ray absorption spectroscopy using *IFEFFIT*, *J. Synchrotron Radiat.*, 12(2005), No. 4, p. 537.
[36] T. Luangwanta, A. Chachvalvutikul, and S. Kaowphong, Facile synthesis and enhanced photocatalytic activity of a novel $FeVO_4/Bi_4O_5Br_2$ heterojunction photocatalyst through step-scheme charge transfer mechanism, *Colloids Surf. A*, 627(2021), art. No. 127217.
[37] C. Holder and R.E. Schaak, Tutorial on powder X-ray diffraction for characterizing nanoscale materials, *ACS Nano*, 13(2019), No. 7, p. 7359.
[38] T. Gholam, L.R. Zheng, J.O. Wang, H.J. Qian, R. Wu, and H.Q. Wang, Synchrotron X-ray absorption spectroscopy study of local structure in Al-doped $BiFeO_3$ powders, *Nanoscale Res. Lett.*, 14(2019), No. 1, art. No. 137.
[39] Z.J. Huang, Z.X. Wang, X.B. Zheng, *et al*., Structural and electrochemical properties of Mg-doped nickel based cathode materials $LiNi_{0.6}Co_{0.2}Mn_{0.2-x}Mg_xO_2$ for lithium ion batteries, *RSC Adv.*, 5(2015), No. 108, p. 88773.
[40] L.N. Xu, J. Li, H.B. Sun, *et al*., *In situ* growth of Cu_2O/CuO nanosheets on Cu coating carbon cloths as a binder-free electrode for asymmetric supercapacitors, *Front. Chem.*, 7(2019), art. No. 420.
[41] Y.H. Wen, G.P. Cao, J. Cheng, and Y.S. Yang, Correlation of capacitance with the pore structure for nanoporous glassy carbon electrodes, *J. Electrochem. Soc.*, 152(2005), No. 9, art. No.

A1770.
[42] V.D. Nithya, R.K. Selvan, C. Sanjeeviraja, D.M. Radheep, and S. Arumugam, Synthesis and characterization of $FeVO_4$ nanoparticles, *Mater. Res. Bull.*, 46(2011), No. 10, p. 1654.
[43] B. Issa, I.M. Obaidat, B.A. Albiss, and Y. Haik, Magnetic nanoparticles: Surface effects and properties related to biomedicine applications, *Int. J. Mol. Sci.*, 14(2013), No. 11, p. 21266.
[44] Y.C. Si, G.N. Liu, C.H. Deng, W. Liu, H.H. Li, and L. Tang, Facile synthesis and electrochemical properties of amorphous $FeVO_4$ as cathode materials for lithium secondary batteries, *J. Electroanal. Chem.*, 787(2017), p. 19.
[45] L.C. Meng, R.S. Guo, X.H. Sun, *et al*., Enhanced electrochemical performance of a promising anode material $FeVO_4$ by tungsten doping, *Ceram. Int.*, 46(2020), No. 13, p. 21360.
[46] K.A. Owusu, L. Qu, J. Li, *et al*., Low-crystalline iron oxide hydroxide nanoparticle anode for high-performance supercapacitors, *Nat. Commun.*, 8(2017), art. No. 14264.
[47] T. Putjuso, S. Putjuso, A. Karaphun, P. Moontragoon, I. Kotutha, and E. Swatsitang, Influence of Co doping on phase, structure and electrochemical properties of hydrothermally obtained $Co_xZn_{1-x}Fe_2O_4$ (x = 0.0–0.4) nanoparticles, *Sci. Rep.*, 13(2023), art. No. 2531.
[48] J. Yan, J.P. Liu, Z.J. Fan, T. Wei, and L.J. Zhang, High-performance supercapacitor electrodes based on highly corrugated graphene sheets, *Carbon*, 50(2012), No. 6, p. 2179.
[49] J. Khajonrit, N. Prasoetsopha, T. Sinprachim, P. Kidkhunthod, S. Pinitsoontorn, and S. Maensiri, Structure, characterization, and magnetic/electrochemical properties of Ni-doped $BiFeO_3$nanoparticles, *Adv. Nat. Sci. Nanosci. Nanotechnol.*, 8(2017), No. 1, art. No. 015010.
[50] V.D. Nithya, R. Kalai Selvan, D. Kalpana, L. Vasylechko, and C. Sanjeeviraja, Synthesis of Bi_2WO_6 nanoparticles and its electrochemical properties in different electrolytes for pseudocapacitor electrodes, *Electrochim. Acta*, 109(2013), p. 720.
[51] A. Mishra, G. Bera, P. Mal, *et al*., Comparative electrochemical analysis of rGO-$FeVO_4$ nanocomposite and $FeVO_4$ for supercapacitor application, *Appl. Surf. Sci.*, 488(2019), p. 221.
[52] V.D. Nithya, K. Pandi, Y.S. Lee, and R.K. Selvan, Synthesis, characterization and electrochemical performances of nanocrystalline $FeVO_4$ as negative and $LiCoPO_4$ as positive electrode for asymmetric supercapacitor, *Electrochim. Acta*, 167(2015), p. 97.
[53] A. George, S. Rahul, A. Dhayal Raj, Q.Q. Yang, C. Sridevi, and J. Madona, Surfactant-assisted hydrothermal synthesis of $FeVO_4$ nanoparticles for supercapacitor applications, *Can. J. Chem*., (2024). DOI: 10.1139/cjc-2024-0080
[54] X.S. Feng, Y. Huang, X.F. Chen, C. Wei, X. Zhang, and M.H. Chen, Hierarchical $CoFe_2O_4$/$NiFe_2O_4$ nanocomposites with enhanced electrochemical capacitive properties, *J. Mater. Sci.*, 53(2018), No. 4, p. 2648.